SINTEF
PROCEEDINGS
2

Proceedings of the 12th International Conference on Computational Fluid Dynamics in the Oil & Gas, Metallurgical and Process Industries

Progress in Applied CFD – CFD2017

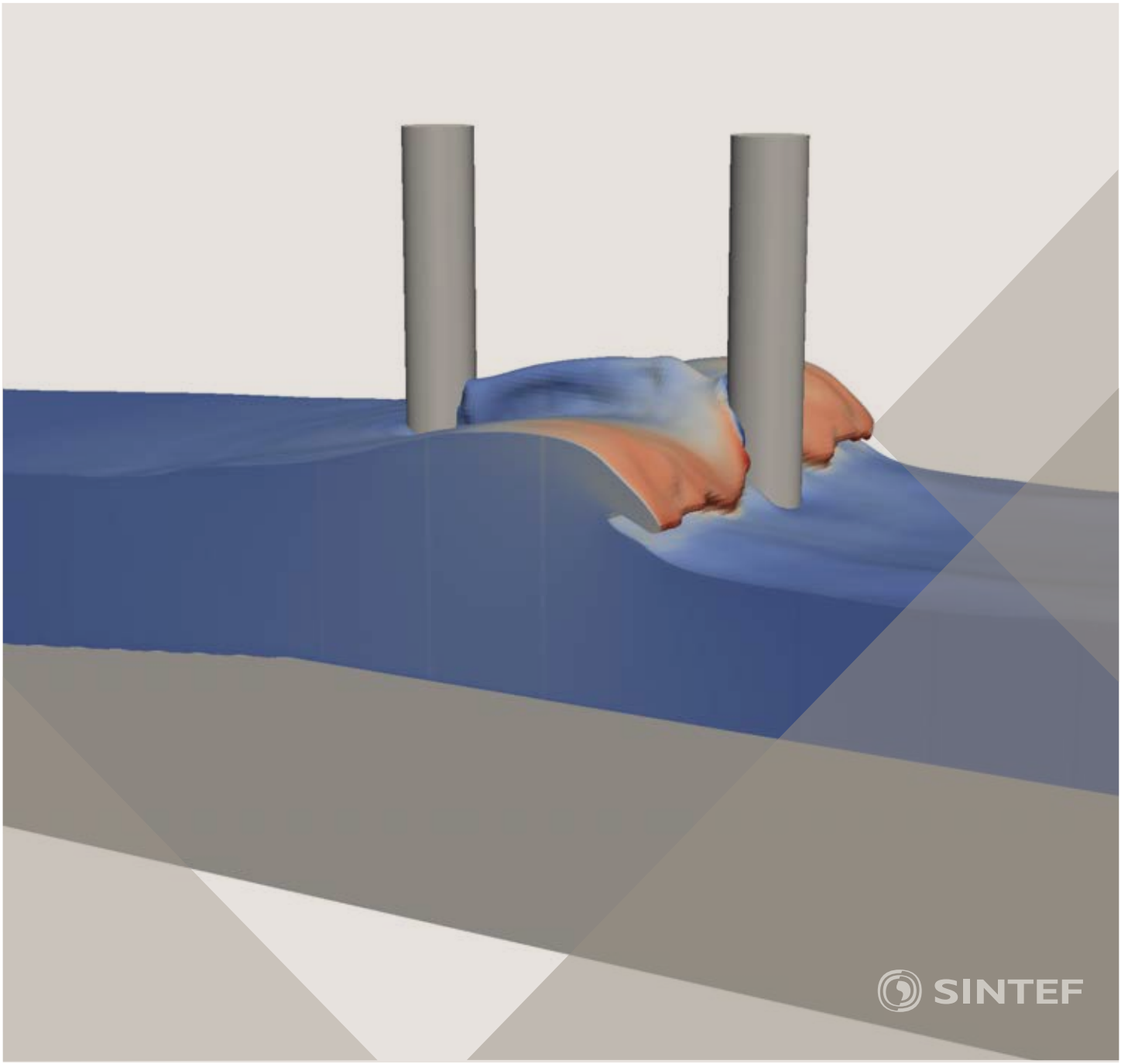

SINTEF Proceedings

Editors:
Jan Erik Olsen and Stein Tore Johansen

Progress in Applied CFD – CFD2017

Proceedings of the 12th International Conference on Computational Fluid Dynamics in the Oil & Gas, Metallurgical and Process Industries

SINTEF Academic Press

SINTEF Proceedings no 2
Editors: Jan Erik Olsen and Stein Tore Johansen
Progress in Applied CFD – CFD2017
Selected papers from 10th International Conference on Computational Fluid Dynamics in the Oil & Gas, Metallurgical and Process Industries

Key words:
CFD, Flow, Modelling

Cover, illustration: Arun Kamath

ISSN 2387-4295 (online)
ISBN 978-82-536-1544-8 (pdf)

SINTEF Academic Press
Address: Forskningsveien 3 B
PO Box 124 Blindern
N-0314 OSLO
Tel: +47 73 59 30 00
Fax: +47 22 96 55 08

www.sintef.no/byggforsk
www.sintefbok.no

SINTEF Proceedings
SINTEF Proceedings is a serial publication for peer-reviewed conference proceedings on a variety of scientific topics.
The processes of peer-reviewing of papers published in SINTEF Proceedings are administered by the conference organizers and proceedings editors. Detailed procedures will vary according to custom and practice in each scientific community.

PREFACE

This book contains all manuscripts approved by the reviewers and the organizing committee of the 12th International Conference on Computational Fluid Dynamics in the Oil & Gas, Metallurgical and Process Industries. The conference was hosted by SINTEF in Trondheim in May/June 2017 and is also known as CFD2017 for short. The conference series was initiated by CSIRO and Phil Schwarz in 1997. So far the conference has been alternating between CSIRO in Melbourne and SINTEF in Trondheim. The conferences focuses on the application of CFD in the oil and gas industries, metal production, mineral processing, power generation, chemicals and other process industries. In addition pragmatic modelling concepts and bio-mechanical applications have become an important part of the conference. The papers in this book demonstrate the current progress in applied CFD.

The conference papers undergo a review process involving two experts. Only papers accepted by the reviewers are included in the proceedings. 108 contributions were presented at the conference together with six keynote presentations. A majority of these contributions are presented by their manuscript in this collection (a few were granted to present without an accompanying manuscript).

The organizing committee would like to thank everyone who has helped with review of manuscripts, all those who helped to promote the conference and all authors who have submitted scientific contributions. We are also grateful for the support from the conference sponsors: ANSYS, SFI Metal Production and NanoSim.

Stein Tore Johansen & Jan Erik Olsen

Organizing committee:

Conference chairman: Prof. Stein Tore Johansen
Conference coordinator: Dr. Jan Erik Olsen
Dr. Bernhard Müller
Dr.Sigrid Karstad Dahl
Dr.Shahriar Amini
Dr.Ernst Meese
Dr.Josip Zoric
Dr.Jannike Solsvik
Dr.Peter Witt

Scientific committee:

Stein Tore Johansen, SINTEF/NTNU
Bernhard Müller, NTNU
Phil Schwarz, CSIRO
Akio Tomiyama, Kobe University
Hans Kuipers, Eindhoven University of Technology
Jinghai Li, Chinese Academy of Science
Markus Braun, Ansys
Simon Lo, CD-adapco
Patrick Segers, Universiteit Gent
Jiyuan Tu, RMIT
Jos Derksen, University of Aberdeen
Dmitry Eskin, Schlumberger-Doll Research
Pär Jönsson, KTH
Stefan Pirker, Johannes Kepler University
Josip Zoric, SINTEF

CONTENTS

PRAGMATIC MODELLING 9
On pragmatism in industrial modeling. Part III: Application to operational drilling 11
CFD modeling of dynamic emulsion stability 23
Modelling of interaction between turbines and terrain wakes using pragmatic approach 29

FLUIDIZED BED 37
Simulation of chemical looping combustion process in a double looping fluidized bed reactor with cu-based oxygen carriers 39
Extremely fast simulations of heat transfer in fluidized beds 47
Mass transfer phenomena in fluidized beds with horizontally immersed membranes 53
A Two-Fluid model study of hydrogen production via water gas shift in fluidized bed membrane reactors 63
Effect of lift force on dense gas-fluidized beds of non-spherical particles 71
Experimental and numerical investigation of a bubbling dense gas-solid fluidized bed 81
Direct numerical simulation of the effective drag in gas-liquid-solid systems 89
A Lagrangian-Eulerian hybrid model for the simulation of direct reduction of iron ore in fluidized beds 97
High temperature fluidization - influence of inter-particle forces on fluidization behavior 107
Verification of filtered two fluid models for reactive gas-solid flows 115

BIOMECHANICS 123
A computational framework involving CFD and data mining tools for analyzing disease in cartoid artery 125
Investigating the numerical parameter space for a stenosed patient-specific internal carotid artery model 133
Velocity profiles in a 2D model of the left ventricular outflow tract, pathological case study using PIV and CFD modeling 139
Oscillatory flow and mass transport in a coronary artery 147
Patient specific numerical simulation of flow in the human upper airways for assessing the effect of nasal surgery 153
CFD simulations of turbulent flow in the human upper airways 163

OIL & GAS APPLICATIONS 169
Estimation of flow rates and parameters in two-phase stratified and slug flow by an ensemble Kalman filter 171
Direct numerical simulation of proppant transport in a narrow channel for hydraulic fracturing application 179
Multiphase direct numerical simulations (DNS) of oil-water flows through homogeneous porous rocks 185
CFD erosion modelling of blind tees 191
Shape factors inclusion in a one-dimensional, transient two-fluid model for stratified and slug flow simulations in pipes 201
Gas-liquid two-phase flow behavior in terrain-inclined pipelines for wet natural gas transportation 207

NUMERICS, METHODS & CODE DEVELOPMENT 213
Innovative computing for industrially-relevant multiphase flows 215
Development of GPU parallel multiphase flow solver for turbulent slurry flows in cyclone 223
Immersed boundary method for the compressible Navier–Stokes equations using high order summation-by-parts difference operators 233
Direct numerical simulation of coupled heat and mass transfer in fluid-solid systems 243
A simulation concept for generic simulation of multi-material flow, using staggered Cartesian grids 253
A cartesian cut-cell method, based on formal volume averaging of mass, momentum equations 265
SOFT: a framework for semantic interoperability of scientific software 273

POPULATION BALANCE 279
Combined multifluid-population balance method for polydisperse multiphase flows 281
A multifluid-PBE model for a slurry bubble column with bubble size dependent velocity, weight fractions and temperature 285
CFD simulation of the droplet size distribution of liquid-liquid emulsions in stirred tank reactors 295
Towards a CFD model for boiling flows: validation of QMOM predictions with TOPFLOW experiments 301
Numerical simulations of turbulent liquid-liquid dispersions with quadrature-based moment methods 309
Simulation of dispersion of immiscible fluids in a turbulent couette flow 317
Simulation of gas-liquid flows in separators - a Lagrangian approach 325
CFD modelling to predict mass transfer in pulsed sieve plate extraction columns 335

BREAKUP & COALESCENCE 343
Experimental and numerical study on single droplet breakage in turbulent flow 345
Improved collision modelling for liquid metal droplets in a copper slag cleaning process 355
Modelling of bubble dynamics in slag during its hot stage engineering 365
Controlled coalescence with local front reconstruction method 373

BUBBLY FLOWS 381
Modelling of fluid dynamics, mass transfer and chemical reaction in bubbly flows 383
Stochastic DSMC model for large scale dense bubbly flows 391
On the surfacing mechanism of bubble plumes from subsea gas release 399
Bubble generated turbulence in two fluid simulation of bubbly flow 405

HEAT TRANSFER 413
CFD-simulation of boiling in a heated pipe including flow pattern transitions using a multi-field concept 415
The pear-shaped fate of an ice melting front 423
Flow dynamics studies for flexible operation of continuous casters (flow flex cc) 431
An Euler-Euler model for gas-liquid flows in a coil wound heat exchanger 441

NON-NEWTONIAN FLOWS 449
Viscoelastic flow simulations in disordered porous media 451
Tire rubber extrudate swell simulation and verification with experiments 459
Front-tracking simulations of bubbles rising in non-Newtonian fluids 469
A 2D sediment bed morphodynamics model for turbulent, non-Newtonian, particle-loaded flows 479

METALLURGICAL APPLICATIONS 491
Experimental modelling of metallurgical processes 493
State of the art: macroscopic modelling approaches for the description of multiphysics phenomena within the electroslag remelting process 499
LES-VOF simulation of turbulent interfacial flow in the continuous casting mold 507
CFD-DEM modelling of blast furnace tapping 515
Multiphase flow modelling of furnace tapholes 521
Numerical predictions of the shape and size of the raceway zone in a blast furnace 531
Modelling and measurements in the aluminium industry - Where are the obstacles? 541
Modelling of chemical reactions in metallurgical processes 549
Using CFD analysis to optimise top submerged lance furnace geometries 555
Numerical analysis of the temperature distribution in a martensic stainless steel strip during hardening 565
Validation of a rapid slag viscosity measurement by CFD 575
Solidification modeling with user defined function in ANSYS Fluent 583
Cleaning of polycyclic aromatic hydrocarbons (PAH) obtained from ferroalloys plant 587
Granular flow described by fictitious fluids: a suitable methodology for process simulations 593
A multiscale numerical approach of the dripping slag in the coke bed zone of a pilot scale Si-Mn furnace 599

INDUSTRIAL APPLICATIONS 605
Use of CFD as a design tool for a phospheric acid plant cooling pond 607
Numerical evaluation of co-firing solid recovered fuel with petroleum coke in a cement rotary kiln: Influence of fuel moisture 613
Experimental and CFD investigation of fractal distributor on a novel plate and frame ion-exchanger 621

COMBUSTION 631
CFD modeling of a commercial-size circle-draft biomass gasifier 633
Numerical study of coal particle gasification up to Reynolds numbers of 1000 641
Modelling combustion of pulverized coal and alternative carbon materials in the blast furnace raceway 647
Combustion chamber scaling for energy recovery from furnace process gas: waste to value 657

PACKED BED 665
Comparison of particle-resolved direct numerical simulation and 1D modelling of catalytic reactions in a packed bed 667
Numerical investigation of particle types influence on packed bed adsorber behaviour 675
CFD based study of dense medium drum separation processes 683
A multi-domain 1D particle-reactor model for packed bed reactor applications 689

SPECIES TRANSPORT & INTERFACES 699
Modelling and numerical simulation of surface active species transport - reaction in welding processes 701
Multiscale approach to fully resolved boundary layers using adaptive grids 709
Implementation, demonstration and validation of a user-defined wall function for direct precipitation fouling in Ansys Fluent 717

FREE SURFACE FLOW & WAVES 727
Unresolved CFD-DEM in environmental engineering: submarine slope stability and other applications 729
Influence of the upstream cylinder and wave breaking point on the breaking wave forces on the downstream cylinder 735
Recent developments for the computation of the necessary submergence of pump intakes with free surfaces 743
Parallel multiphase flow software for solving the Navier-Stokes equations 752

PARTICLE METHODS 759
A numerical approach to model aggregate restructuring in shear flow using DEM in Lattice-Boltzmann simulations 761
Adaptive coarse-graining for large-scale DEM simulations 773
Novel efficient hybrid-DEM collision integration scheme 779
Implementing the kinetic theory of granular flows into the Lagrangian dense discrete phase model 785
Importance of the different fluid forces on particle dispersion in fluid phase resonance mixers 791
Large scale modelling of bubble formation and growth in a supersaturated liquid 798

FUNDAMENTAL FLUID DYNAMICS 807
Flow past a yawed cylinder of finite length using a fictitious domain method 809
A numerical evaluation of the effect of the electro-magnetic force on bubble flow in aluminium smelting process 819
A DNS study of droplet spreading and penetration on a porous medium 825
From linear to nonlinear: Transient growth in confined magnetohydrodynamic flows 831

CONTROLLED COALESCENCE WITH LOCAL FRONT RECONSTRUCTION METHOD

A. H. RAJKOTWALA[1]*, H. MIRSANDI[1], E. A. J. F. PETERS[1], M. W. BALTUSSEN[1], C. W. M. VAN DER GELD [2], J. G. M. KUERTEN[3], J. A. M. KUIPERS[1]

[1]Multiphase Reactors Group, Department of Chemical Engineering and Chemistry, Eindhoven University of Technology, P.O. Box 513, 5600 MB Eindhoven, The Netherlands

[2]Process and Product Design Group, Department of Chemical Engineering and Chemistry, Eindhoven University of Technology, P.O. Box 513, 5600 MB Eindhoven, The Netherlands

[3]Multiphase and Reactive Flows Group, Department of Mechanical Engineering, Eindhoven University of Technology, P.O. Box 513, 5600 MB Eindhoven, The Netherlands

* E-mail: a.rajkotwala@tue.nl

ABSTRACT

The physics of droplet collisions involves a wide range of length scales. This poses a difficulty to accurately simulate such flows with traditional fixed grid methods due to their inability to resolve all scales with affordable number of computational grid cells. A solution is to couple a fixed grid method with simplified sub grid models that account for microscale effects. In this paper, we incorporate such framework in the Local Front Reconstruction Method (Shin *et al.*, 2011). To validate the new method, simulations of (near) head on collision of two equal tetradecane droplets are carried out at different Weber numbers corresponding to different collision regimes. The results show a better agreement with experimental data compared to other fixed grid methods like Front Tracking (Pan *et al.*, 2008) and Coupled Level Set and Volume of Fluid (CLSVOF) (Kwakkel *et al.*, 2013), especially at high impact velocities.

Keywords: Numerical Simulation, Multiphase flows, Front Tracking, LFRM, coalescence, break-up, droplet collision.

NOMENCLATURE

Greek Symbols

ρ	Mass density, $[kg/m^3]$.
μ	Dynamic viscosity, $[kg/ms]$.
σ	Surface tension coefficient, $[N/m]$.

Latin Symbols

p	Pressure, [Pa].
$\mathbf{u}$	Fluid Velocity, $[m/s]$.
$\mathbf{g}$	Gravitational acceleration, $[m/s^2]$.
$\mathbf{F}_\sigma$	Surface tension force, $[N/m^3]$.
t	time, [s].
$\mathbf{n}$	Surface normal.
t_c	Contact time between droplets, [s].
t_d	Film drainage time, [s].
R_0	Initial droplet radius, [m].
V_0	Initial droplet speed, $[m/s]$.
b	Offset distance between droplets, [m].

Sub/superscripts

Γ	Interface.
l	Liquid.

INTRODUCTION

Droplet-laden flows play an important role in many industrial applications and natural processes (Crowe *et al.*, 1998). Some examples are spraying of fuel in combustion engines, spray drying of food products, liquid-liquid extraction, growth of rain droplets in clouds and pollution tracking. The interaction between droplets has a major influence on the dynamics of such flows, because of the coalescence and break-up that may occur upon collision. However, it is very difficult to accurately capture coalescence and break-up numerically because of the wide range of length scales involved. For example, the collision dynamics of droplets is influenced by the drainage of the thin gas film separating two colliding droplets (Mason *et al.*, 2012), causing bouncing of the droplets when the film is not drained during the collision event. Coalescence occurs when the gas film ruptures. The rupture is attributed to the van der Waals surface forces which become dominant at nanometer scale. It is not possible to capture all scales ranging from millimeter (droplet diameter) to nanometer (critical film thickness) using an affordable number of computational grid cells.

In our fixed grid method, the under resolved final stage of the film drainage process is accounted for by a sub-grid model. Few studies have been done previously using different fixed grid methods and sub-grid models (Kwakkel *et al.*, 2013, Mason *et al.*, 2012). The fixed grid methods for modeling multiphase flows can be divided into two types: front capturing and front tracking techniques (Tryggvason *et al.*, 2011). In front capturing methods, the interface is implicitly represented by a colour function. Common front capturing methods are Volume of Fluid (VOF) (van Sint Annaland *et al.*, 2005), Level Set (LS) (Sethian and Smereka, 2003) and Coupled Level Set and Volume of Fluid (CLSVOF) (van der Pijl *et al.*, 2005) methods. Generally, the droplets in these methods coalesce automatically when they share a common grid cell. However, this numerical coalescence can be avoided for the simulation of symmetric binary droplet collision using Volume of Fluid method. The coalescence can be controlled by prescribing a volume-fraction boundary condition on the collision plane using ghost cells (Mason *et al.*, 2012). When the boundary condition is set to zero volume fraction, the droplets will bounce; whereas a symmetry boundary condition will result in coalescence. A more general approach to avoid numerical coalescence is to use unique colour function for each droplet (Nikolopoulos *et al.*, 2009).

A big disadvantage of front capturing methods is the very fine grid resolution which is required for accurate surface

tension calculation especially when the droplets undergo complex topological changes (Kwakkel *et al.*, 2013). Front tracking methods (Dijkhuizen *et al.*, 2010, Shin *et al.*, 2011) are inherently better at surface tension calculation at coarse grid resolution. This is because a front tracking method directly tracks the interfaces using triangular marker elements, enabling accurate curvature calculation. However, in the traditional front tracking method, droplet coalescence is not possible. To incorporate coalescence, additional routines to merge the individual unstructured meshes belonging to different droplets are required (Nobari *et al.*, 1996). In the traditional front tracking method, the merging of the droplet meshes is complicated because the logical information about the marker connectivity should be updated. In addition, the merging of droplets with complex topology is very challenging. Therefore, we choose a front tracking method without connectivity, the Local Front Reconstruction Method (LFRM) by Shin *et al.*, 2011.

As logical connectivity between marker elements is not required, LFRM can handle complex topological changes like droplet coalescence and pinch off. It uses information from the original marker elements directly to reconstruct the interface in a mass conservative manner and thus, also ensures good local mass conservation. Because the interface is reconstructed independently in each individual reconstruction cell, the method can be highly parallelized. However, this cell-oriented reconstruction leads to numerical coalescence (similar to front capturing methods) in LFRM (Shin *et al.*, 2011). This is prevented in our implementation by storing the information about marker elements and marker points for each droplet separately. The coalescence is accomplished by merging data-structures of two droplets. Similarly, the break-up of a droplet is done by splitting the data-structure of the droplet. The details of these procedures are given in next section. We have improved the original LFRM method in certain areas which are also summarized in next section. Lastly, the results of simulations of (near) head on collision of two equal tetradecane droplets in different collision regimes are discussed. The discussion includes validation of simulations with experimental data and comparison with other fixed grid methods (Kwakkel *et al.*, 2013, Pan *et al.*, 2008).

METHODOLOGY

Local Front Reconstruction Method

Both fluids in the two phase flow are assumed to be incompressible, immiscible and Newtonian fluids. A one-fluid formulation is used and the governing equations are given by the continuity equations and the Navier-Stokes equations, where the physical properties depend on local phase fractions.

$$\nabla \cdot \mathbf{u} = 0 \tag{1}$$

$$\rho \frac{\partial \mathbf{u}}{\partial t} + \rho \nabla \cdot (\mathbf{u}\mathbf{u}) = -\nabla p + \rho \mathbf{g} + \nabla \cdot \mu \left[\nabla \mathbf{u} + (\nabla \mathbf{u})^T \right] + \mathbf{F}_\sigma \tag{2}$$

where $\mathbf{F}_\sigma$ is a singular source-term to represent the surface tension at the interface.

The following conditions are applied at the interface Γ to close the governing equations:

$$[\mathbf{u}]_\Gamma = 0 \tag{3}$$

$$\left[-p\mathbf{n} + \mu \left(\nabla \mathbf{u} + (\nabla \mathbf{u})^T \right) \cdot \mathbf{n} \right]_\Gamma = \mathbf{S}_\sigma \cdot \mathbf{n} \tag{4}$$

where $[.]_\Gamma$ represents jump in a quantity across the interface from one phase to another and $\mathbf{S}_\sigma$ is the surface force acting on interface due to surface tension.

The equations are discretized using a finite volume approach and are solved on a staggered computational grid by a fractional step method (Das *et al.*, 2017). The surface tension force $\mathbf{F}_\sigma$ is calculated using hybrid surface tension model (Shin *et al.*, 2005) which has combined advantage of accurate curvature calculation (similar to the pull force model which is commonly used in front tracking methods) and proper balance of pressure and surface tension force at discrete level (similar to the continuum surface model which is commonly used in front capturing methods).

The fluid velocity is interpolated from Eulerian grid to Lagrangian grid using cubic spline interpolation and marker points are moved with the interpolated velocity using a 4^{th} order Runge-Kutta scheme (Dijkhuizen *et al.*, 2010).

As mentioned before, the local phase fraction is required to calculate the averaged physical properties. This can be calculated by the geometric analysis using the positions of the marker points (Dijkhuizen *et al.*, 2010). This method of phase fraction calculation is exact and computationally more efficient than the traditional method of solving Poisson equation used in original LFRM method. From the calculated phase fractions, the average density and viscosity is calculated by algebraic and harmonic averaging, respectively.

Due to the advection of the marker points, the marker elements can become too large or too small. This poor grid quality decreases the accuracy of the surface tension force calculation. To maintain the mesh quality, a mesh reconstruction procedure of (Shin *et al.*, 2011) is implemented. The reconstruction procedure also allows to reconstruct the mesh when the multiple droplets coalesce or a droplet breaks-up. The implementation is improved by the use of linked-list data-structures for storing location of the three vertices of each marker. This ensures that each marker point has a unique identity, thus reducing the memory requirements and preventing precision problems.

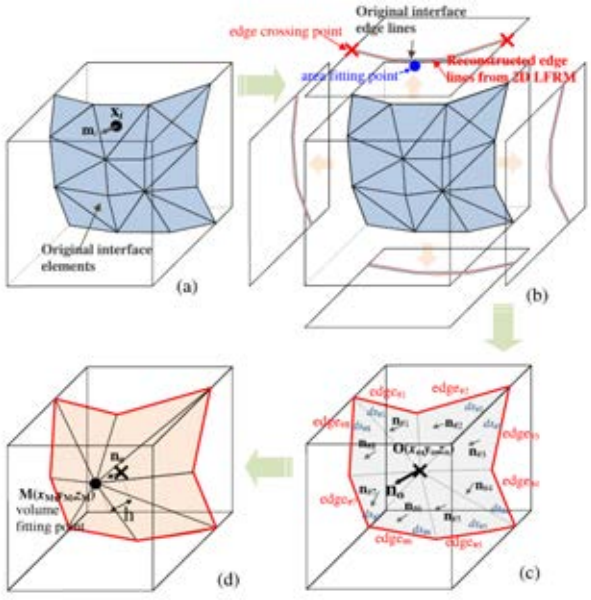

Figure 1: Schematic of the reconstruction procedure for LFRM (Shin *et al.*, 2011).

The overall reconstruction procedure consists of four simple steps as shown in Figure 1:

(a) Localization - Interface of the discrete phase is cut by a reconstruction grid (similar to the Eulerian grid) such that each part of the interface lies completely inside one cell.

(b) Edge line reconstruction - The edge line corresponding to the cut interface is traced out on relevant faces of the cell, and new edge line (containing only two edge points and a fitting point) is reconstructed in an area conservative manner.

(c) Centroid calculation - Using edge points and fitting points of all the faces, a centroid is calculated. An intermediate interface is formed by connecting the centroid with intermediate edge lines.

(d) Volume fitting - Finally, the centroid is moved in the normal direction of intermediate interface such that original volume of the dispersed phase is conserved in the given cell.

Flows involving coalescence and break-up of the dispersed phase are easily handled by LFRM. This is enabled by the marker reduction and the tetra-marching procedures, which allow merging and breaking of unstructured meshes of the dispersed phase. Details of these procedures can be found in (Shin *et al.*, 2011). In our implementation, the data-structure of each droplet is stored with a unique identity. However, this prevents coalescence completely. To enable coalescence between two droplets at a desired time, their data-structures have to be merged and the merged droplet has to be given a unique identifier, which is handled by the coalescence module. Similarly, each daughter droplet is given a unique identifier when formed after break-up of a droplet, which is handled by the break-up module.

Coalescence Module

The coalescence module checks if there are multiple interfaces within the same reconstruction cell and combines the data-structures of two droplets depending on the calculated film drainage and contact time. The different steps in the coalescence module are given below:

(a) Bounding box for droplets in terms of grid cell units is calculated (Figure 2(a)).

(b) At each time step, it is checked if the bounding boxes of any two droplets are overlapping.

(c) If the overlap exists, the cells containing interfaces from both droplets are flagged to check if any cell contains interface from both droplets (Figure 2(b)).

(d) If one or more cells contain interface from both droplets, then these droplets are identified to be in 'contact' and added to a collision list (Figure 2(c)). The contact timer is initiated to keep track of contact time t_c.

(e) At each time step, it is checked if the droplets pair is still in contact. If a pair is in contact, the contact time is compared to the film drainage time t_d. In this study, the film drainage time t_d is obtained from experiments. If the contact exists and $t_c > t_d$, the data-stuctures of two droplets are merged and reconstruction is performed to execute droplet coalescence (Figure 2(e)). If the contact ceases, the droplets are removed from the collision list and this leads to bouncing of droplets.

Break-up Module

The numerical break-up of the droplet will take place based on the size of the reconstruction grid. As stated before, it is important to separate the data-structure of the droplets after break-up to avoid numerical coalescence. This separation is achieved by using a recursive flagging algorithm. The algorithm is used to find the disjoint droplets that are subsequently assigned a new 'droplet-number', see Figure 3.

RESULTS

In case of (near) head-on collisions between equal sized hydrocarbon droplets, four regimes of collision outcome are observed with increasing Weber number (measure of droplet inertia compared to surface tension). As seen in Figure 4, these regimes are (I) Coalescence with minor deformation, (II) Bouncing, (III) Coalescence with major deformation and (IV) Coalescence with separation resulting in production of daughter droplets. To validate the modified LFRM method, a

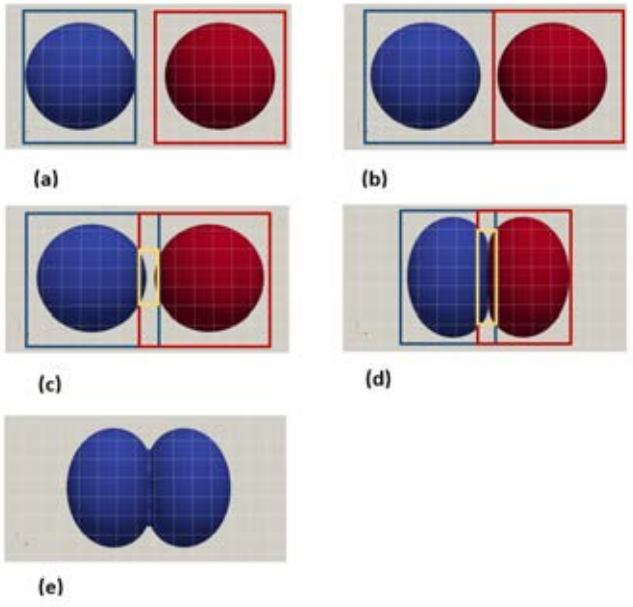

Figure 2: Schematic of the coalescence module. Blue and red boxes represent bounding boxes of blue and red droplets respectively. Yellow box represents cells containing interface from both droplets.

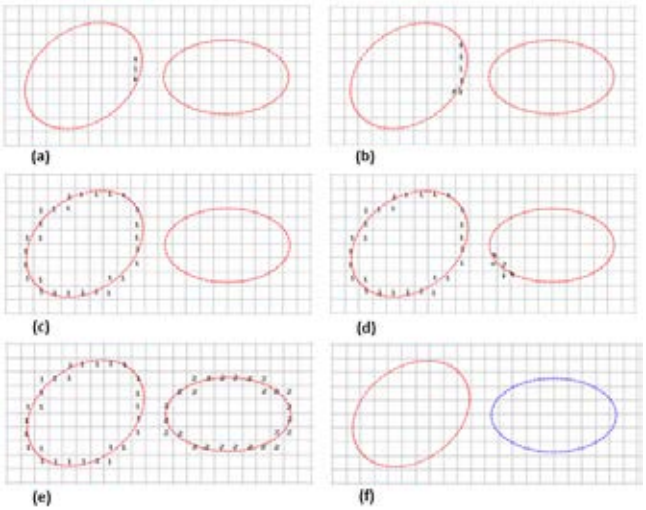

Figure 3: Steps of flagging algorithm in the break-up module.

case of binary droplet collision from each of these regimes is simulated and compared with experiments (Pan *et al.*, 2008 and Qian and Law, 1997) and other simulation methods (Pan *et al.*, 2008 and Kwakkel *et al.*, 2013).

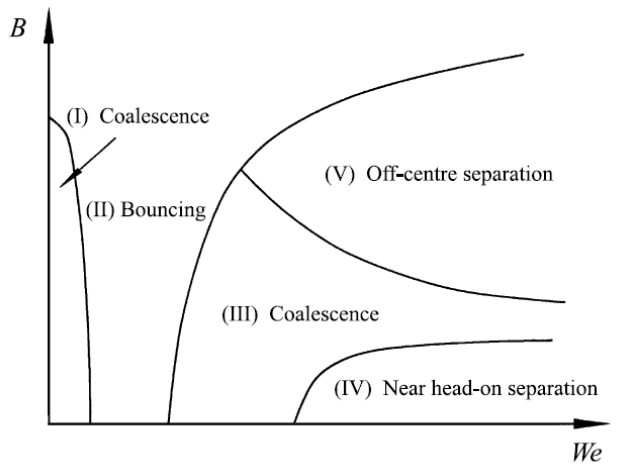

Figure 4: Schematic of collision regimes of two equal sized hydrocarbon droplets in atmospheric pressure. The parameter B represents the obliqueness of the collision and We represents the Weber number (Qian and Law, 1997).

The grid cell size is selected such that 12 grid cells are taken across the droplet radius (R_0) (similar to grid size used in (Kwakkel *et al.*, 2013) for CLSVOF and (Pan *et al.*, 2008) for FT). The computational domain has dimensions $8R_0 \times 10R_0 \times 8R_0$ with the largest dimension in the direction of the collision. Free slip boundary condition is used on all domain boundaries. The initial distance between the droplet centers is taken as $2.8R_0$. Each droplet is initialised with a uniform velocity field, V_0, but in the opposite direction. For each case, Weber number and impact parameter (Figure 5) are provided as an input. The film drainage time is provided by experimental observations (Pan *et al.*, 2008).

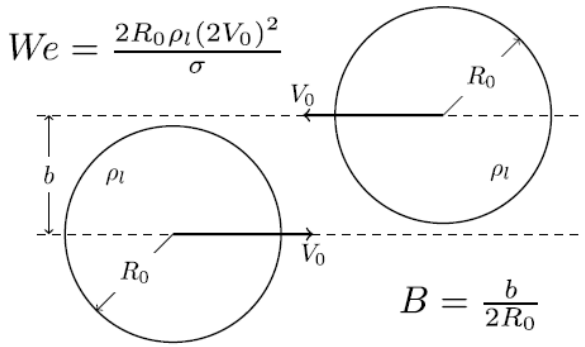

Figure 5: Nomenclature of general binary droplet collision (Kwakkel *et al.*, 2013).

Regime I

This regime always results in coalescence, while the collisions are gentle (low Weber numbers). A collision of tetradecane droplets in 1 atm. air, $R_0 = 107.2\,\mu$m , $V_0 = 0.305$ m/s, $We = 2.3$, and $B = 0$ is shown in Figure 6. The obtained result from LFRM matches well with results from the Coupled Level Set Volume of Fluid method (Kwakkel *et al.*, 2013), the Front Tracking method (Pan *et al.*, 2008) and experimental data (Pan *et al.*, 2008). In such regime, the coalescence happens around maximum deformation. After the coalescence, the cusp at the merged interface is quickly flattened. This phenomenon is nicely captured by all the numerical simulations.

Regime II

This regime always results in bouncing. A collision of tetradecane droplets in 1 atm. air, $R_0 = 167.6\,\mu$m, $V_0 = 0.492$ m/s, $We = 9.33$, and $B = 0$ is shown in Figure 7. Again, the results obtained using LFRM agree well with experimental data (Pan *et al.*, 2008) and other simulation results with FT (Pan *et al.*, 2008) and CLSVOF (Kwakkel *et al.*, 2013).

Regime III

This regime always results in coalescence, however the collisions are hard collision (high weber numbers) resulting in substantial deformation before merging. A collision of tetradecane droplets in 1 atm. air, $R_0 = 169.7\,\mu$m, $V_0 = 0.591$ m/s, $We = 13.63$, and $B = 0$ is shown in Figure 8. The merging in this case occurs as the deformed droplet is flattened to a disk shape while the incoming mass at the center of the rear face is still heading forward resulting in dimpled shape between 370 and 500 ms. Although this is not very clear in the experimental results (Pan *et al.*, 2008) but it was captured properly by all the numerical simulations.

Regime IV

This regime of near head on collision results in separation of droplets after merging as the kinetic energy is sufficient to overcome the surface energy. A collision of tetradecane droplets in 1 atm. nitrogen, $R_0 = 168\,\mu$m, $V_0 = 1.260$ m/s, $We = 62.2$, and $B = 0.06$ is shown in Figure 9. A zero film drainage time (which is justified by high weber number) is used in the simulation. The different colour of droplets indicate that each droplet has different droplet number and separate data-structure.

The results obtained using LFRM match better with the experimental results (Qian and Law, 1997) compared to the CLSVOF (Kwakkel *et al.*, 2013). In Figure 9, a premature separation is seen for CLSVOF. As explained in (Kwakkel *et al.*, 2013), the origin of this premature separation is the less accurate curvature estimation in strongly deformed regions. These errors in curvature estimation have a direct consequence for the acting surface tension force, and over time the droplet shape. This indicates that LFRM has more accurate surface tension calculation for the same grid size. Also, the size of the satellite droplet resembles the experimental data better compared to the CLSVOF results.

CONCLUSION

The local front reconstruction method has been improved and extended to allow for controlled coalescence. The new method has been successfully validated by carrying out simulations of binary (near) head on droplet collisions. By using experimentally observed film drainage times, a good match with experimental data is observed. This shows that if an accurate predictions of the film drainage time can be obtained from a sub-grid model, LFRM can capture collision dynamics in multiphase flows with physical realism. Finally, the results obtained using LFRM are compared with those of other methods and a better agreement with experimental data is seen, especially at high impact velocities.

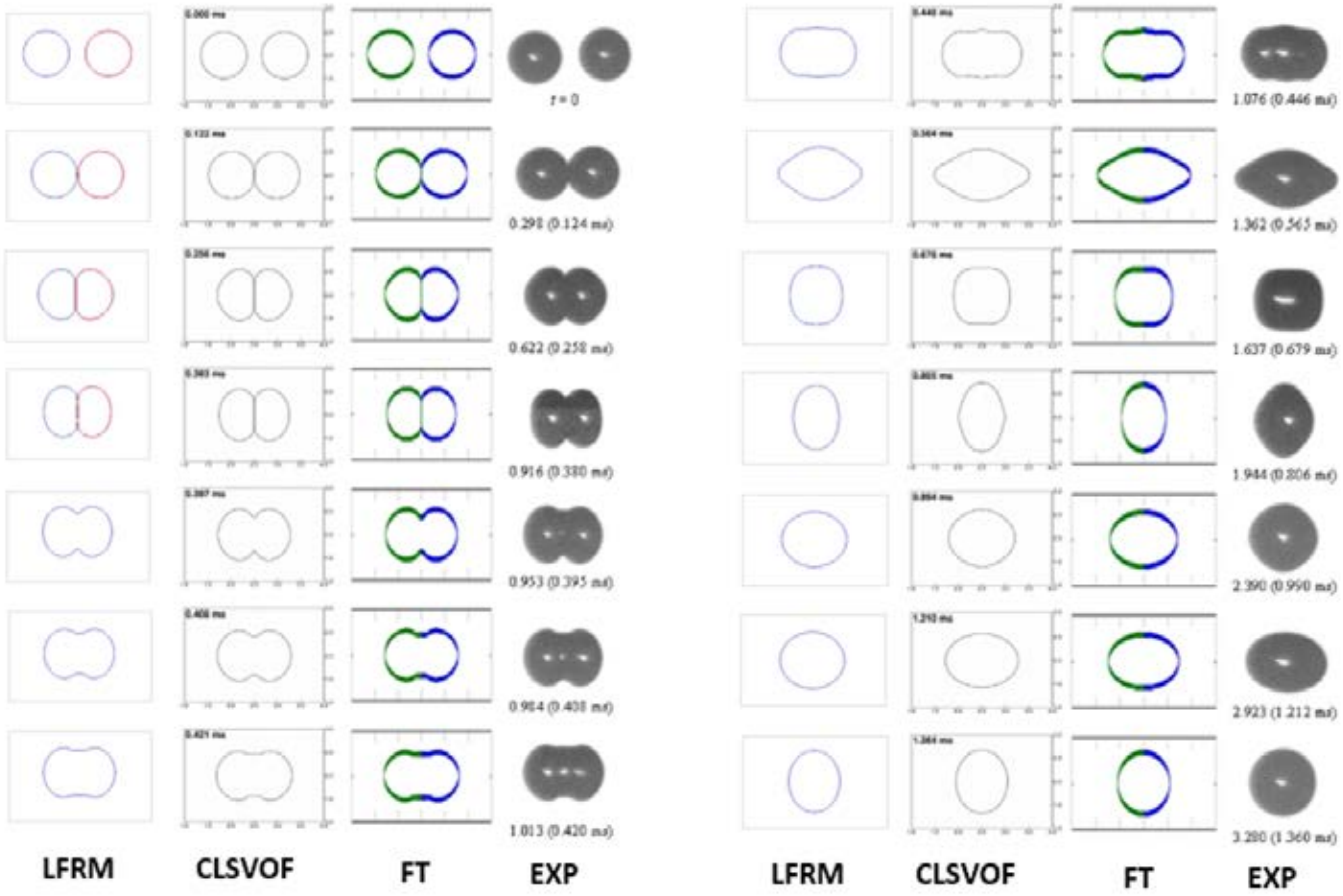

Figure 6: Merging collision sequence in regime I. LFRM results from present study, CLSVOF from (Kwakkel *et al.*, 2013), FT and experimental results from (Pan *et al.*, 2008). Conditions: tetradecane in 1 atm. air, $R_0 = 107.2\,\mu$m, $V_0 = 0.305$ m/s, $We = 2.3$, and $B = 0$. The film drainage time observed in experiments is $t_d = 0.270$ ms.

ACKNOWLEDGEMENT

This work is part of the research programme Open Technologieprogramma with project number 13781, which is (partly) financed by the Netherlands Organisation for Scientific Research (NWO) Domain Applied and Engineering Sciences (TTW, previously Technology Foundation STW).

REFERENCES

CROWE, C., SOMMERFELD, M. and TSUJI, Y. (1998). *Multiphase flows with droplets and particles*. CRC Press, Boca Raton.

DAS, S., DEEN, N.G. and KUIPERS, J.A.M. (2017). "Immersed boundary method (ibm) based direct numerical simulation of open-cell solid foams: Hydrodynamics". *AIChE Journal*, **63(3)**, 1152–1173.

DIJKHUIZEN, W., ROGHAIR, I., ANNALAND, M.V.S. and KUIPERS, J. (2010). "DNS of gas bubbles behaviour using an improved 3d front tracking model - model development". *Chemical Engineering Science*, **65(4)**, 1427 – 1437.

KWAKKEL, M., BREUGEM, W.P. and BOERSMA, B.J. (2013). "Extension of a CLSVOF method for droplet-laden flows with a coalescence/breakup model". *Journal of Computational Physics*, **253**, 166 – 188.

MASON, L., STEVENS, G. and HARVIE, D. (2012). "Multi-scale volume of fluid modelling of droplet coalescence". *Ninth International Conference on CFD in the Minerals and Process Industries*. CSIRO, Melbourne, Australia.

NIKOLOPOULOS, N., NIKAS, K.S. and BERGELES, G. (2009). "A numerical investigation of central binary collision of droplets". *Computers & Fluids*, **38(6)**, 1191 – 1202.

NOBARI, M.R., JAN, Y.J. and TRYGGVASON, G. (1996). "Headon collision of drops - a numerical investigation". *Physics of Fluids*, **8(1)**, 29–42.

PAN, K.L., LAW, C.K. and ZHOU, B. (2008). "Experimental and mechanistic description of merging and bouncing in head-on binary droplet collision". *Journal of Applied Physics*, **103(6)**, 064901.

QIAN, J. and LAW, C. (1997). "Regimes of coalescence and separation in droplet collision". *Journal of Fluid Mechanics*, **331**, 59–80.

SETHIAN, J.A. and SMEREKA, P. (2003). "Level set methods for fluid interfaces". *Annual Review of Fluid Mechanics*, **35(1)**, 341–372.

SHIN, S., ABDEL-KHALIK, S.I., DARU, V. and JURIC, D. (2005). "Accurate representation of surface tension using the level contour reconstruction method". *J. Comput. Phys.*, **203(2)**, 493–516.

SHIN, S., YOON, I. and JURIC, D. (2011). "The local front reconstruction method for direct simulation of two- and three-dimensional multiphase flows". *Journal of Computational Physics*, **230(17)**, 6605 – 6646.

TRYGGVASON, G., SCARDOVELLI, R. and ZALESKI, S. (2011). *Direct Numerical Simulations of Gas-Liquid Multiphase Flows*. Cambridge University Press, Cambridge.

VAN DER PIJL, S., SEGAL, A., VUIK, C. and WESSELING, P. (2005). "A mass-conserving Level-Set method for modelling of multi-phase flows". *International Journal for*

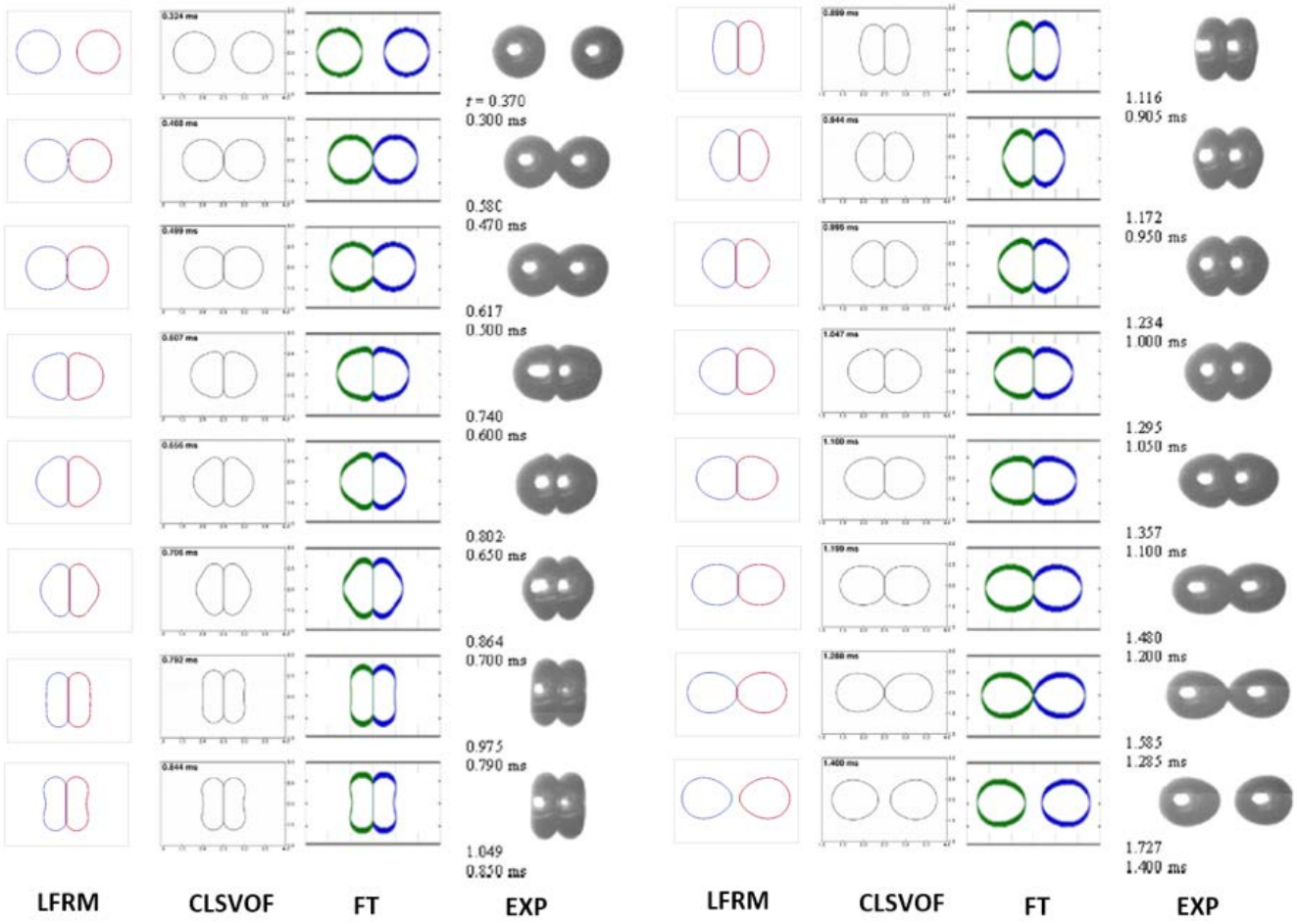

Figure 7: Bouncing collision sequence in regime II. LFRM results from present study, CLSVOF from (Kwakkel *et al.*, 2013), FT and experimental results from (Pan *et al.*, 2008). Conditions: tetradecane in 1 atm. air, $R_0 = 167.6\,\mu$m, $V_0 = 0.492$ m/s, $We = 9.33$, and $B = 0$.

Numerical Methods in Fluids, **47**, 339–361.

VAN SINT ANNALAND, M., DEEN, N. and KUIPERS, J. (2005). "Numerical simulation of gas bubbles behaviour using a three-dimensional volume of fluid method". *Chemical Engineering Science*, **60(11)**, 2999–3011.

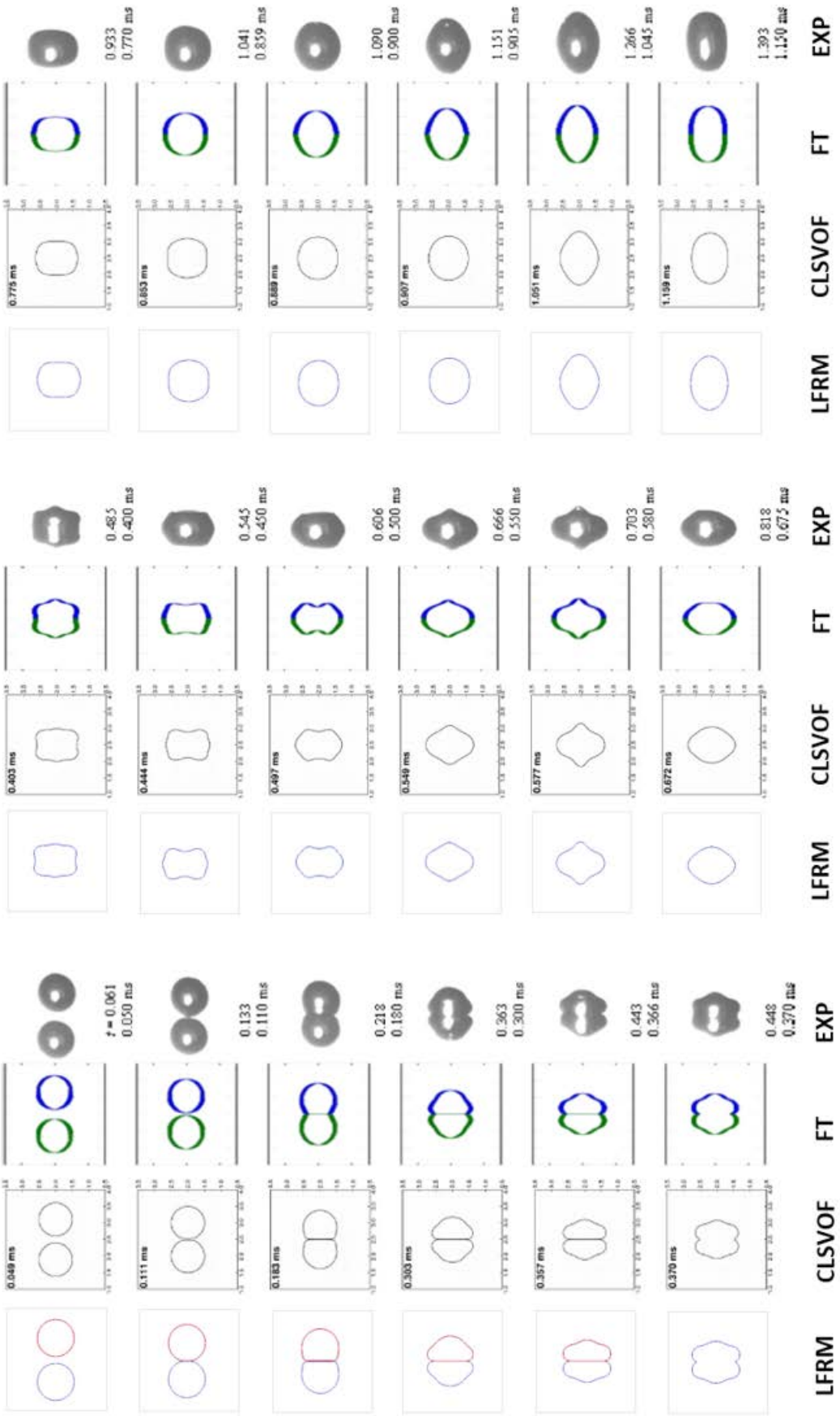

Figure 8: Merging collision sequence in regime III. LFRM results from present study, CLSVOF from (Kwakkel *et al.*, 2013), FT and experimental results from (Pan *et al.*, 2008). Conditions: tetradecane in 1 atm. air, $R_0 = 169.7$ µm, $V_0 = 0.591$ m/s, $We = 13.63$, and $B = 0$. The film drainage time observed in experiments is $t_d = 0.246$ ms.

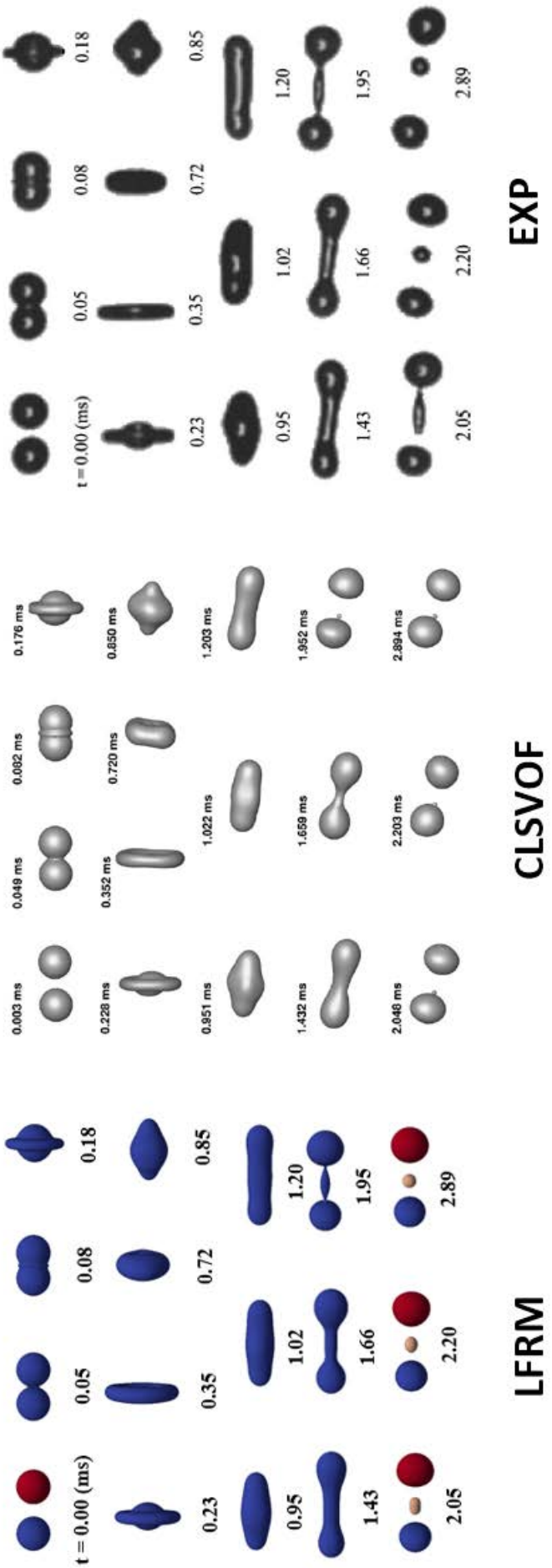

Figure 9: Near head on separating collision sequence in regime IV. LFRM results from present study, CLSVOF from (Kwakkel *et al.*, 2013) and experimental results from (Qian and Law, 1997). Conditions: tetradecane in 1 atm. nitrogen, $R_0 = 168\,\mu$m, $V_0 = 1.260$ m/s, $We = 62.2$, and $B = 0.06$. The film drainage time is assumed to be zero.